


ORIGINAL ARTICLE

Open Access

Nonlinear Control of Magnetically Coupled Rodless Cylinder Position Servo System



Yeming Zhang^{1,2}, Demin Kong¹, Gonghua Jin¹, Yan Shi^{3*} , Maolin Cai³, Shuping Li¹ and Baozhan Lv¹

Abstract

Magnetically coupled rodless cylinders are widely used in the coordinate positioning of mechanical arms, electrostatic paintings, and other industrial applications. However, they exhibit strong nonlinear characteristics, which lead to low servo control accuracy. In this study, a mass-flow equation through the valve port was derived to improve the control performance, considering the characteristics of the dynamics and throttle-hole flow. Subsequently, a friction model combining static, viscous, and Coulomb friction with a zero-velocity interval was proposed. In addition, energy and dynamic models were set for the experimental investigation of the magnetically coupled rodless cylinder. A nonlinear mathematical model for the position of the magnetically coupled rodless cylinder was proposed. An incremental PID controller was designed for the magnetically coupled rodless cylinder to control this system, and the PID parameters were adjusted online using RBF neural network. The response results of the PID parameters based on the RBF neural network were compared with those of the traditional incremental PID control, which proved the superiority of the optimization control algorithm of the incremental PID parameters based on the RBF neural network servo control system. The experimental results of this model were compared with the simulation results. The average error between the established model and the actual system was 0.005175054 (m), which was approximately 2.588% of the total travel length, demonstrating the accuracy of the theoretical model.

Keywords Magnetically coupled rodless cylinder, Nonlinear model, Position control, Radial basis function neural network (RBF-NN), Neural network (NN)

1 Introduction

In an automatic control system, the output of the pneumatic servo system can be changed based on the input of the target signal. It consists of an air compressor, electric pneumatic control components, pneumatic actuators, and sensors. Based on different controlled variables, pneumatic servo control systems can be classified into

speed, position, force, and position–force composite control systems.

In cases in which the precision of the pneumatic position servo control is not high, traditional point-to-point control can satisfy general engineering requirements. However, improved pneumatic position servo control technology is required for high-precision pneumatic position servo control. The reasons that affect the precision of pneumatic position servo control are as follows. The pneumatic system exhibits nonlinear characteristics and model uncertainty. If the mathematical model of a pneumatic nonlinear dynamic system is linearized near the ideal working position, the kinematic and dynamic analysis of the system will lose practical significance when the motion state of the system model significantly deviates from the ideal working point. This type of linearized system structure is extremely simple, and the

*Correspondence:

Yan Shi

shiyian@buaa.edu.cn

¹ School of Mechanical and Power Engineering, Henan Polytechnic University, Jiaozuo 454000, China

² State Key Laboratory of Fluid Power and Mechatronic Systems, Zhejiang University, Hangzhou 310027, China

³ School of Automation Science and Electrical Engineering, Beihang University, Beijing 100191, China



© The Author(s) 2023. **Open Access** This article is licensed under a Creative Commons Attribution 4.0 International License, which permits use, sharing, adaptation, distribution and reproduction in any medium or format, as long as you give appropriate credit to the original author(s) and the source, provide a link to the Creative Commons licence, and indicate if changes were made. The images or other third party material in this article are included in the article's Creative Commons licence, unless indicated otherwise in a credit line to the material. If material is not included in the article's Creative Commons licence and your intended use is not permitted by statutory regulation or exceeds the permitted use, you will need to obtain permission directly from the copyright holder. To view a copy of this licence, visit <http://creativecommons.org/licenses/by/4.0/>.

control precision of the system cannot attain the ideal control effect. Therefore, it is necessary to establish a more accurate nonlinear mathematical model for nonlinear problems of pneumatic servo systems [1, 2].

The control approach also influences the precision of pneumatic position servo control. The Selection of an appropriate control strategy can compensate for the motion error of the model and ensure more accurate and efficient position control of the pneumatic servo system [3]. Different types of pneumatic servo systems require appropriate control algorithms to achieve improved performance. Therefore, in recent years, scholars have actively conducted research in this area and achieved good results. Bai [4] investigated the position servo control system of an oscillating cylinder, reduced the instability caused by nonlinear factors using proportional-integral-derivative (PID) control and a pneumatic-assisted limit control algorithm, and improved the position control accuracy. Ren et al. [5] developed an adaptive sliding-mode control method for a pneumatic position-servo control system. An adaptive sliding mode controller was designed using a backstepping method. Its advantage is that it exhibits a good tracking effect when no pressure sensors are used, and the parameters of the dynamic model and the variation range of the model parameters are unknown. Li et al. [6] proposed a hybrid controller comprising a fuzzy-PID controller and a neural network pre-compensator (NNPC) to overcome the nonlinearity and uncertainty caused by air compressibility and temperature variations in the motion control of a pneumatic execution system. The simulation results showed that the tracking effect of the nonlinear fuzzy-PID controller and NNPC combined control was superior. Hsu et al. [7] designed a hybrid fuzzy repetitive control method based on an existing PID closed-loop control system and added a feedforward compensator and zero-phase error-tracking controller to the system. The proposed hybrid control method has a faster convergence rate and lower steady-state error than other control methods. Huang et al. [8] proposed a self-adaptation fuzzy controller to regulate the up-and-down movement of a four-legged pneumatic actuator that exhibited pneumatic characteristics of compressibility, nonlinear delay, and difficulty in establishing a mathematical model of the heavy-duty pneumatic actuator.

This intelligent control strategy, which combines the adaptive rule, fuzzy control algorithm, and sliding-mode control algorithm, has adjustment control parameters and an online learning ability to deal with time-varying and nonlinear uncertainty coupling behavior systems.

Combined with the above problems, the physical structure and mechanical properties of the proportional directional control valve and magnetically coupled rodless cylinder were analyzed. In addition, the quality of the proportional direction valve flow model, magnetically coupled rodless cylinder-type friction model, energy model, and dynamic model for the magnetically coupled rodless cylinder were established. Therefore, a theoretical model of a magnetically coupled nonlinear rodless cylinder position servo system was developed based on these models. Finally, the theoretical and experimental models were compared and analyzed using an incremental PID control algorithm. The average error between the established model and actual system was 0.005175054 (m), which was approximately 2.588% of the total travel. The accuracy of the comparison between the radial basis function (RBF)-tuning incremental PID and incremental PID control algorithms was established in the simulation model. The results showed that the RBF-tuning incremental PID control algorithm improved the position control accuracy of the pneumatic system more than the incremental PID control algorithm in the simulation model.

2 Characteristic Analysis of Proportional Directional Control Valve

The main components of the proportional directional control valve were the electromagnetic control and reversing parts. The MPYE-5-M5-010-B proportional directional control valve developed by Festo consisted of a shell, valve spool, valve spool coil, and control plate. The working principle is that when the input voltage ranges from 0 to 10 V, the displacement of the valve spool is approximately linear with the input voltage [9]. A Panasonic HG-C1050 laser displacement sensor was used for the experiment, and the results indicated that the valve spool displacement of the proportional directional control valve was approximately 2.2 mm on average.

2.1 Derivation of Mass Flow Equation of Proportional Directional Control Valve

The gas flow principle of a valve-controlled cylindrical system is shown in Figure 1. Ports 4 and 2 of the proportional directional control valves are connected to both ends of the magnetically coupled rodless cylinder.

The left and right cavities of the cylinder are assumed to be Cavities A and B, respectively. \dot{M}_a and \dot{M}_b are the mass flow rates of gas in two cavities of the cylinder, P_a and P_b are the gas pressures of two cavities of the

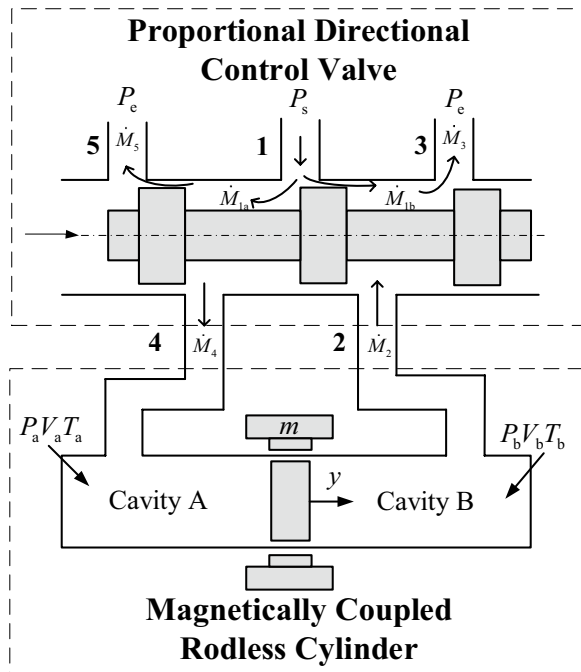


Figure 1 Valve-controlled cylinder system

cylinder, V_a and V_b are the volumes of two cavities of the cylinder, and T_a and T_b are the temperatures of the two cavities of the cylinder. m is the mass of the load, y is the displacement of piston movement in the cylinder, and P_e and P_s are the atmospheric pressure and air-supply pressure, respectively [10].

The following assumptions were made to simplify the mathematical model of the valve-controlled cylinder system [11].

1. The air used in the system is an ideal gas.
2. The gas flow in the proportional directional control valve and cylinder is considered to occur in an isentropic adiabatic state.
3. The pressure and temperature of the gas in the same cavity are equal everywhere.
4. During the back-and-forth movement of the piston in the cylinder, the gas in the two chambers and outside did not undergo heat exchange (adiabatic process).
5. The pressure and temperature of the air supply are unaffected by the external environment and remain constant.

When the valve spool of the proportional directional control valve moves to the right (forward), as shown in Figure 2, the left side of port 1 becomes the throttle hole,

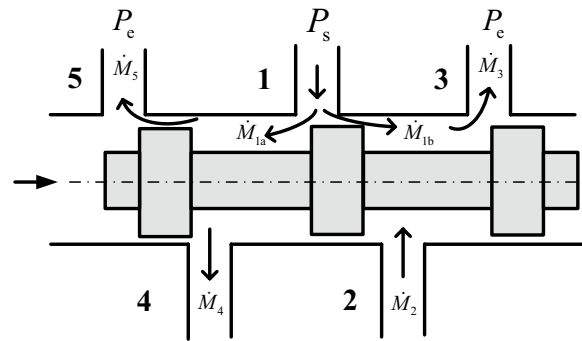


Figure 2 Structure of proportional directional control valve moving to the right

and the right side becomes the gap. Regardless of the left-most and right-most throttles of the valve, ports 5 and 3 become the gap and throttle holes, respectively. After the supply gas enters port 1, most of the gas flows through port 1 to the left side of the valve-body chamber. The gas flowing into the left cavity flows into cavity A of the cylinder through port 4, and a small portion of the gas is discharged from the gap at port 5.

The mass flow of gas \dot{M}_4 through port 4 is assumed to be equal to the mass flow of gas \dot{M}_a into chamber A of the cylinder. Thus, the difference between the mass flow rates of gas \dot{M}_{1a} flowing into port 1 and gas \dot{M}_5 flowing into the atmosphere from port 5 is the mass flow rate of the gas \dot{M}_a in Chamber A of the cylinder.

$$\dot{M}_a = \dot{M}_4 = \dot{M}_{1a} - \dot{M}_5. \tag{1}$$

Similarly, assuming the mass flow rate of the gas \dot{M}_b in Chamber B of the cylinder, the following relationship is valid:

$$\dot{M}_b = \dot{M}_2 = \dot{M}_3 - \dot{M}_{1b}. \tag{2}$$

Because the opening area of the proportional directional control valve port is nonlinear with respect to the control voltage, it cannot be measured directly using effective measurement tools. According to the method proposed in Ref. [4], the volume flow of gas through the valve port is measured, and the volume flow is substituted into Eq. (3) to obtain the effective area of the valve opening:

$$S = \frac{q_v}{0.124P_u} \sqrt{\frac{T_1}{273}}, \tag{3}$$

where S is the effective area of the valve opening (mm^2), P_u is the absolute pressure upstream of the valve body

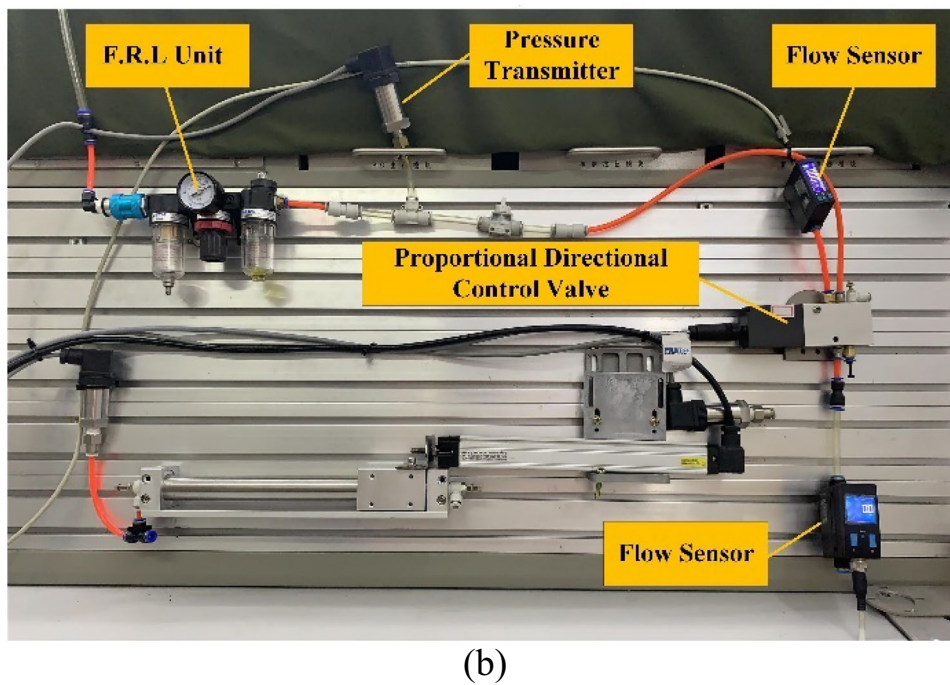
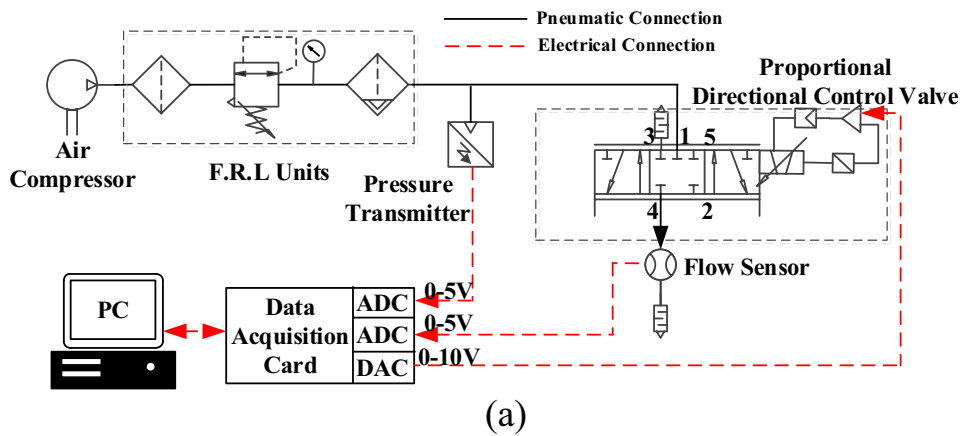


Figure 3 Experimental platform: (a) Structural representation, (b) Laboratory equipment

(Pa), T_1 is the temperature upstream of the valve body (K), and q_v is the volume flow through the valve port (L/min).

The experimental platform was set up, as shown in Figure 3.

The inlet and outlet on the right side of the proportional directional control valve were plugged, and the air supply pressure was set to 0.5 MPa. The control voltage was adjusted from 0 to 10 V and from 10 to 0 V as a cycle voltage. The volume flows through proportional

directional control valve port 4 at different control voltages were measured.

Similarly, the left inlet and outlet of the valve were blocked, and the volume flow rate of valve port 2 was measured using the same cycle voltage. The entire experiment was repeated three times, and the results of each experiment were added and averaged. The results are presented in Figure 4.

The data were then substituted into Eq. (3), and the mathematical expression of the fitting curve of the

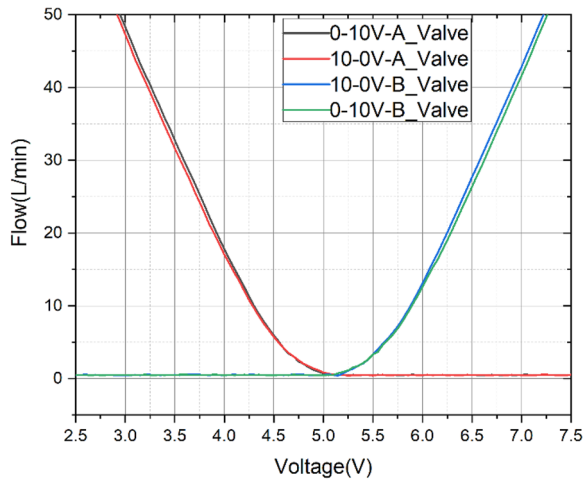


Figure 4 Volume flow through proportional directional control valve port under cycle voltage

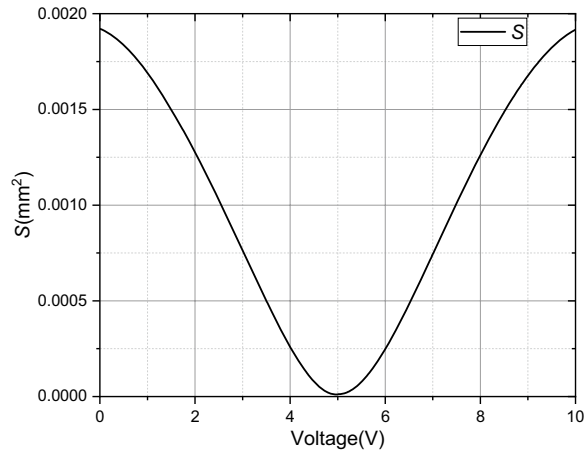


Figure 5 Relationship between effective area of valve opening and input voltage

relationship between the effective area of valve port 1 and the control voltage is as follows:

$$S = \frac{0.4881\sqrt{Temp}}{P_s} * (5.7036 * volt + 12.7755 * volt^2 - 2.2893 * volt^3 + 0.0820 * volt^4). \tag{4}$$

The relationship between the effective opening area and voltage was plotted, as shown in Figure 5.

According to Wu [12] and Bai [4], the mass flow equations of the gas flowing through the throttle hole are expressed by Eqs. (5) and (6):

$$\dot{M}_{1a} = \begin{cases} \frac{CSP_s}{\sqrt{RT_s}} \sqrt{\frac{2\kappa}{\kappa-1} \left[\left(\frac{P_a}{P_s}\right)^{\frac{2}{\kappa}} - \left(\frac{P_a}{P_s}\right)^{\frac{\kappa+1}{\kappa}} \right]}, & \left(\frac{P_a}{P_s}\right) \geq b, \\ \frac{CSP_s}{\sqrt{RT_s}} \sqrt{\frac{2\kappa}{\kappa+1} \left(\frac{2}{\kappa+1}\right)^{\frac{2}{\kappa-1}}}, & \left(\frac{P_a}{P_s}\right) < b, \end{cases} \tag{5}$$

$$\dot{M}_3 = \begin{cases} \frac{CSP_b}{\sqrt{RT_b}} \sqrt{\frac{2\kappa}{\kappa-1} \left[\left(\frac{P_e}{P_b}\right)^{\frac{2}{\kappa}} - \left(\frac{P_e}{P_b}\right)^{\frac{\kappa+1}{\kappa}} \right]}, & \left(\frac{P_e}{P_b}\right) \geq b, \\ \frac{CSP_b}{\sqrt{RT_b}} \sqrt{\frac{2\kappa}{\kappa+1} \left(\frac{2}{\kappa+1}\right)^{\frac{2}{\kappa-1}}}, & \left(\frac{P_e}{P_b}\right) < b, \end{cases} \tag{6}$$

where R is the gas constant with a value of $8.31432 \times 10^3 \text{ N}\cdot\text{m}/(\text{kg}\cdot\text{K})$, b is the critical pressure ratio with a value of $b = 0.528$, T_b is the temperature of Cavity B, T_s is the air supply temperature, and κ is the isentropic index with a value of $\kappa = 1.4$. Because of the environmental influence, correction parameter C is introduced to modify the equation, whose values can be obtained from experimental data.

2.2 Flow Analysis of Small-hole Mass Flow of Proportional Directional Control Valve

The state of gas flow in the gap of the proportional directional control valve is similar to that between the two parallel panels. Figure 6 shows the gas flow near port 5 when the valve spool of the proportional directional control valve is moved to the right.

Based on the differential equation of pressure [13] of gas flowing between parallel plates, Eq. (7) is expressed as follows:

$$\frac{dP}{dx} = -\mu \frac{d^2u}{dz^2}, \tag{7}$$

where dP is the pressure of gas element in the clearance, μ is the viscosity coefficient of the gas with a value of $0.0000183 \text{ Pa}\cdot\text{s}$, u is the velocity of gas element in x -direction, L_0 is the initial length of the clearance with

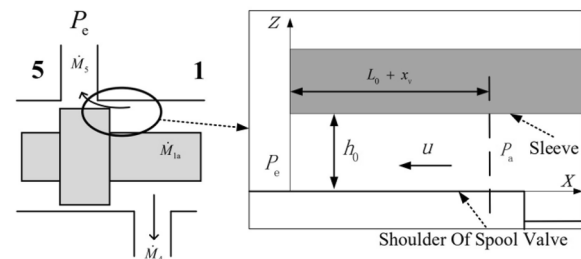


Figure 6 Gas flow near port 5 of proportional directional valve

a value of 0.002 m, x_v is the displacement of the valve spool, and h_0 is the distance between the sleeve and the shoulder of the spool valve.

The boundary conditions are as follows:

$$\begin{cases} \text{If } z = 0, & \text{then } u = 0, \\ \text{If } z = h_0, & \text{then } u = 0, \end{cases} \quad (8)$$

$$\begin{cases} \text{If } x = 0, & \text{then } p = p_e, \\ \text{If } x = L_0 + x_v, & \text{then } p = p_a. \end{cases} \quad (9)$$

By combining Eqs. (7) and (8), the equation of velocity of the gas flow in the gap is expressed as follows.

$$u = -\frac{1}{2\mu} \frac{dP}{dx} z(z - h_0). \quad (10)$$

The mass flow of gas at port 5 is expressed by Eq. (11):

$$\dot{M}_5 = \rho_e \int_0^{h_0} u \cdot \pi d_s dz. \quad (11)$$

where ρ_e is the density of the gas.

Because the clearance size of the parallel plate is fixed in x -direction, the gas pressure of the clearance gradually increases with an increase in x -axis. From Eqs. (7) and (9), Eq. (12) is derived:

$$\frac{dP}{dx} = \frac{P_a - P_e}{L_0 + x_v}. \quad (12)$$

Based on the equation of state of gas under ideal conditions [14], Eq. (13) is derived:

$$P_e = \rho_e RT_a. \quad (13)$$

From Eqs. (10)–(13), the mathematical expression for the mass flow rate of gas flowing through port 5 can be obtained as follows:

$$\begin{aligned} \dot{M}_5 &= \frac{P_e}{RT_a} \int_0^{h_0} -\frac{1}{2\mu} \cdot \frac{P_a - P_e}{L_0 + x_v} \cdot z(z - h_0) \cdot \pi d_s dz \\ &= \frac{\pi d_s h_0^3 P_e (P_a - P_e)}{12\mu(L_0 + x_v)RT_a} = \frac{\pi d_s (d_h - d_s)^3 P_e (P_a - P_e)}{96\mu(L_0 + x_v)RT_a}. \end{aligned} \quad (14)$$

Similarly, the mathematical expression for M_{1b} is defined by Eq. (15):

$$\dot{M}_{1b} = \frac{\pi d_s (d_h - d_s)^3 P_b (P_s - P_b)}{96\mu(L_0 + x_v)RT_s}. \quad (15)$$

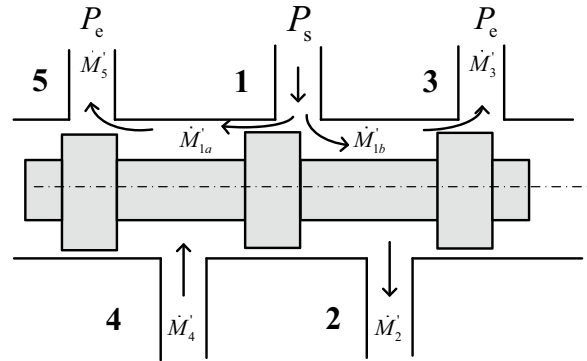


Figure 7 Moving the proportional directional valve spool backward

2.3 Derivation of Mass Flow Equation for Reverse Movement of Spool

Figure 7 shows the process of moving the spool of the proportional directional control valve backward (to the left).

Similarly, the mass flow equation for each port gas is expressed as follows:

$$\dot{M}'_a = \dot{M}'_5 - \dot{M}'_{1a}, \quad (16)$$

$$\dot{M}'_b = \dot{M}'_{1b} - \dot{M}'_3. \quad (17)$$

The mass flow equations of the gas flowing through the throttle hole are as follows:

$$\dot{M}'_5 = \begin{cases} \frac{CSP_a}{\sqrt{RT_a}} \sqrt{\frac{2\kappa}{\kappa - 1} \left[\left(\frac{P_e}{P_a} \right)^{\frac{2}{\kappa}} - \left(\frac{P_e}{P_a} \right)^{\frac{\kappa+1}{\kappa}} \right]}, & \left(\frac{P_e}{P_a} \geq b \right), \\ \frac{CSP_a}{\sqrt{RT_a}} \sqrt{\frac{2\kappa}{\kappa + 1} \left(\frac{2}{\kappa + 1} \right)^{\frac{2}{\kappa-1}}}, & \left(\frac{P_e}{P_a} < b \right), \end{cases} \quad (18)$$

$$\dot{M}'_{1b} = \begin{cases} \frac{CSP_s}{\sqrt{RT_s}} \sqrt{\frac{2\kappa}{\kappa - 1} \left[\left(\frac{P_b}{P_s} \right)^{\frac{2}{\kappa}} - \left(\frac{P_b}{P_s} \right)^{\frac{\kappa+1}{\kappa}} \right]}, & \left(\frac{P_b}{P_s} \geq b \right), \\ \frac{CSP_s}{\sqrt{RT_s}} \sqrt{\frac{2\kappa}{\kappa + 1} \left(\frac{2}{\kappa + 1} \right)^{\frac{2}{\kappa-1}}}, & \left(\frac{P_b}{P_s} < b \right), \end{cases} \quad (19)$$

where T_b is the temperature of cavity B.

The mass flow equations of the gas flowing through the gap are as follows:

$$\dot{M}'_{1a} = \frac{\pi d_s (d_h - d_s)^3 P_a (P_s - P_a)}{96\mu(L_0 - x_v)RT_s}, \quad (20)$$

$$\dot{M}'_3 = \frac{\pi d_s (d_h - d_s)^3 P_e (P_b - P_e)}{96\mu(L_0 - x_v)RT_b}, \quad (21)$$

where \dot{M}' is the mass flow of each port of the valve in reverse.

3 Characteristic Analysis of Magnetically Coupled Rodless Cylinder

3.1 Friction Analysis of Magnetically Coupled Rodless Cylinder

Among the numerous existing static friction models, the most widely used are the Coulomb friction, viscous friction + Coulomb friction, static friction + Coulomb + viscous friction, and Stribeck friction (exponential) models [15].

From a simple and practical perspective, the Coulomb friction + viscous friction + static friction model with a zero-velocity interval was used to describe the friction of the magnetically coupled rodless cylinder [4] analyzed in this study.

Its mathematical description is as follows:

$$F_f = \begin{cases} F_{df} \cdot \text{sgn}(v) + \beta v, & |v| > D_v, \\ F_p \cdot \text{sgn}(v), & |v| \leq D_v \text{ and } F_p < F_{sfmax}, \\ F_{sfmax} \text{sgn}(F_p) \cdot \text{sgn}(v), & |v| \leq D_v \text{ and } F_p \geq F_{sfmax}, \end{cases} \quad (22)$$

where F_p is the driving force generated by the pressure of the two chambers of the cylinder (N), F_f is the friction (N), F_{df} is the Coulomb friction (N), F_{sfmax} is the maximum static frictional force (N), v is the speed (m/s), β

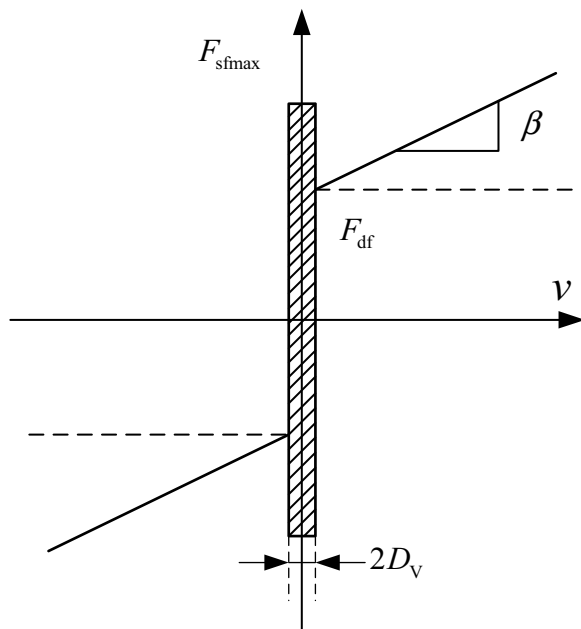


Figure 8 Friction model of Coulomb friction + viscous friction + static friction with zero-velocity interval

is the coefficient of viscous friction (N/(m · s)), D_v is the zero-speed range boundary value (m/s).

Its model is depicted in Figure 8.

When the magnetically coupled rodless cylinder performs a slow and uniformly linear motion, the piston in the magnetically coupled rodless cylinder is only subjected to frictional force and gas pressure in the two cavities of the cylinder; therefore, the frictional force can be calculated using Newton's second law:

$$F_f = A_a P_a - A_b P_b, \quad (23)$$

where A_a and A_b are the Piston areas of cavities A and B of the magnetically coupled rodless cylinder (m²), respectively.

Because the cylinder exhibits a creeping effect in the low-speed section, it can be considered that the creeping of the cylinder is a process in which the pressure slowly

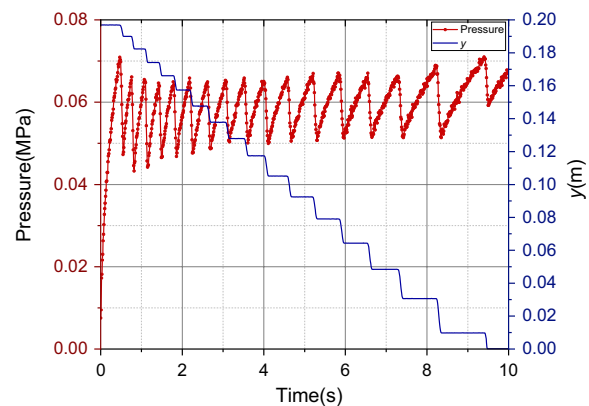


Figure 9 Displacement of cylinder core and pressure variation in cavity A

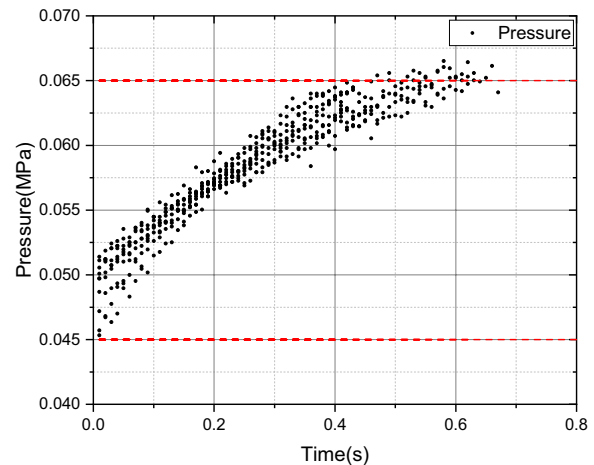


Figure 10 Beginning and end of each crawling

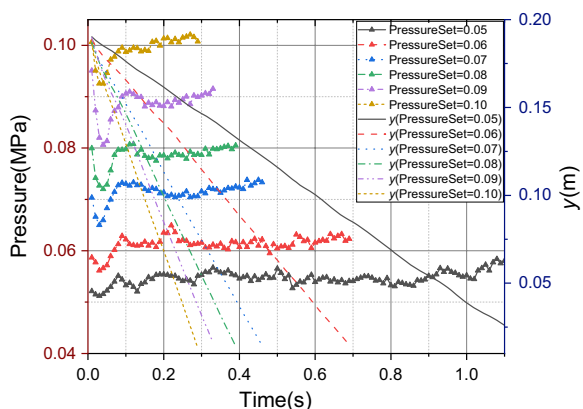


Figure 11 Pressure–displacement–time curve of cylinder

Table 1 Pressure–speed data of cylinder

Pressure (MPa)	Speed (m/s)
0.0536	0.1524
0.0602	0.2555
0.0698	0.382
0.0764	0.4537
0.0865	0.5363
0.0957	0.6075

increases to the maximum static frictional force, slides, and then stops when the pressure decreases to a specific value owing to the expansion of the cylinder cavity. Assuming that cavity A of the cylinder is supplied with air and cavity B is open to connect with atmospheric pressure, displacement and pressure occur, as shown in Figure 9. When the gas enters cavity A, the cylindrical core does not move until the pressure is sufficiently high to cause the core to slide suddenly, and the movement is captured by the sensors. Because of the sliding, cavity A will have a larger volume, which is directed toward lowering the pressure until the cylinder core stops sliding, and the pressure in cavity A will start increasing.

By adopting the end of each section of the cylinder crawling as the starting point and the beginning of the crawling as the end point, the change in the cylinder pressure at the beginning and end of each crawl can be obtained. As shown in Figure 10, the maximum static frictional force acted at 0.065 MPa, and the minimum sliding frictional force acted at 0.045 MPa.

It is necessary to slide the cylinder core at a stable pressure to analyze the relationship between the velocity and friction of the cylinder. When the cavity pressure was set between 0.05 and 0.10 MPa using the PID control method, the real-time pressure and displacement were

Table 2 Friction parameters

Symbol	Value
A (mm ²)	490.87
F_{df} (N)	2.6298
β (N/(m · s))	4.4898
F_{sfmax} (N)	3.1891
D_v (m/s)	0.12

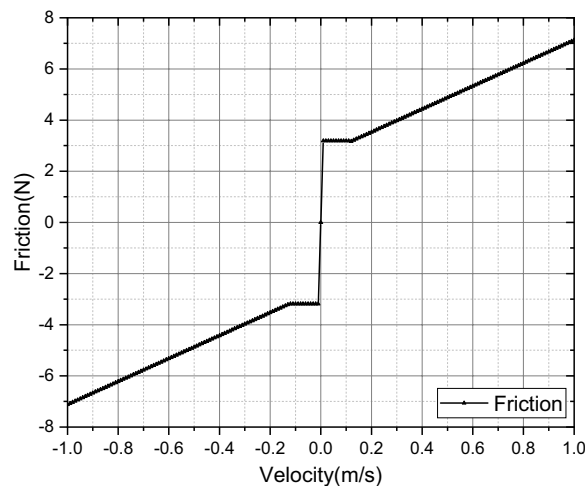


Figure 12 Fitting curve of frictional force for magnetically coupled rodless cylinder

recorded by the sensors. Figure 11 shows the pressure–displacement–time curves.

After linear fitting of the real-time pressure and displacement data, the pressure–speed data were obtained, as listed in Table 1.

In summary, the parameters of the Coulomb friction + viscous friction + static friction model with a zero-velocity interval was obtained, as listed in Table 2.

The fitting curve of the frictional force is shown in Figure 12. The dotted box indicates the area of the static-friction model with a zero-velocity interval.

3.2 Establishment of Energy Equation of Magnetically Coupled Rodless Cylinder

Cavity A of the magnetically coupled rodless cylinder was used as an example to analyze the pressure in the cylinder cavity [16]. In the quasiequilibrium state of an ideal gas, the pressure, temperature, and density of the gas in the cylinder satisfy the following mathematical relationship:

$$\frac{P_a}{\rho_a} = RT_a. \tag{24}$$

By substituting $\rho_a = M_a/V_a$ into Eq. (24), the equation of state of the gas in the cavity can be derived as follows:

$$T_a M_a = \frac{P_a V_a}{R}, \tag{25}$$

where ρ_a is the density of gas in cavity A (kg/m^3), and M_a is the mass of gas in cavity A (kg).

We assume that the gas in the cylinder chamber is always in thermodynamic equilibrium. In other words, when the cylinder is charged and deflated, the state parameters of the gas in the cylinder cavity change over time. According to the first law of thermodynamics, the energy equation of cavity A of the magnetically coupled rodless cylinder is expressed as follows:

$$dQ_a + h_i dM_{ia} = dU_a + dW_a + h_o dM_{oa}, \tag{26}$$

where dQ_a is the heat exchanged between the gas in the cavity and the outside (J); h_i is the energy that flows 1 kg gas by the gas source into the cavity (J/kg); dM_{ia} is the mass of gas entering cavity A (kg); dU_a is the change in the internal energy of all gases in the cavity (J), and h_o is the energy removed by the discharge of 1 kg gas from the gas leisure chamber (J/kg); dW_a is the work performed by all the gases in the chamber (J), and dM_{oa} is the mass of the gas in cavity A at the same time (kg).

Assuming the cylinder is processing the adiabatic movement, and the cavity A is already discharged, the heat exchange with the outside of the cavity is zero. The mass of the gas entering $dM_{ia} = 0$, the reduced mass of the gas in cavity A is the same as the mass of the gas discharged from cavity A; that is, $dM_{oa} = -dM_a$. The change in internal energy in cavity A is dU_a ; the work performed by the gas in cavity A is dW_a , and the energy discharged by the gas in cavity A is $h_o dM_{oa}$. Their expressions are as follows:

$$\begin{cases} dU_a = d(u_a M_a) = c_v d(T_{oa} M_a), \\ dW_a = P_a dV_a, \\ h_o dM_{oa} = (c_v + R) T_{oa} dM_a, \end{cases} \tag{27}$$

where T_{oa} is the temperature of cavity A of the cylinder when deflated. Based on Eq. (26),

$$c_v d(T_{oa} M_a) + P_a dV_a - (c_v + R) T_{oa} dM_a = 0. \tag{28}$$

Substitution of Eq. (25) into Eq. (28) gives Eq. (29):

$$c_v d\left(\frac{P_a V_a}{R}\right) + P_a dV_a - (c_v + R) T_{oa} dM_a = 0. \tag{29}$$

After sorting out Eq. (29), Eq. (30) is obtained:

$$\kappa R T_{oa} dM_a = V_a dP_a + \kappa P_a dV_a. \tag{30}$$

When cavity A of the cylinder is inflated, the internal gas in cavity A does not exchange heat with the outside. That is, $dQ_a = 0$. The mass of the discharged gas is $dM_a = 0$, and the mass of the gas flowing into cavity A is the same as the mass added to cavity A; that is, $dM_{ia} = dM_a$. The change in the internal energy in cavity A is dU_a , the work performed by the gas in cavity A is dW_a , and the energy released by the gas entering cavity A is $h_i dM_{ia}$. Their respective expressions are as follows:

$$\begin{cases} dU_a = d(u_a M_a) = c_v d(T_{ia} M_a), \\ dW_a = P_a dV_a, \\ h_i dM_{ia} = (c_v + R) T_{ia} dM_a, \end{cases} \tag{31}$$

where T_{ia} is the temperature in cavity A when cavity A enters the air.

According to Eqs. (25) and (26), the energy equation for cavity A during inflation is expressed as follows:

$$\kappa R T_{ia} dM_a = V_a dP_a + \kappa P_a dV_a. \tag{32}$$

The gas temperature in the cavity is assumed to be the same as that in the atmosphere to simplify the mathematical model of the system. The energy equation for cavity A during filling and deflating can then be expressed by Eq. (32).

3.3 Derivation of Differential and Dynamic Equations of Pressure in Magnetically Coupled Rodless Cylinder

From Eq. (32), the mass flow equation of cylinder cavity A is derived as follows [17]:

$$\frac{dM_a}{dt} = \frac{V_a}{\kappa T_s R} \frac{dP_a}{dt} + \frac{P_a}{T_s R} \frac{dV_a}{dt}. \tag{33}$$

Similarly, the mass flow equation of cylinder cavity B is derived as follows:

$$\frac{dM_b}{dt} = \frac{V_b}{\kappa T_s R} \frac{dP_b}{dt} + \frac{P_b}{T_s R} \frac{dV_b}{dt}. \tag{34}$$

From Eqs. (1) and (2), the following expression is valid:

$$\begin{cases} \frac{dP_a}{dt} = \frac{\kappa R T_s}{V_a} (\dot{M}_{1a} - \dot{M}_5) - \frac{\kappa P_a}{V_a} \frac{dV_a}{dt}, \\ \frac{dP_b}{dt} = \frac{\kappa R T_s}{V_b} (\dot{M}_{1b} - \dot{M}_3) - \frac{\kappa P_b}{V_b} \frac{dV_b}{dt}. \end{cases} \tag{35}$$

Considering the volumes of the two cavities in the cylinder, $A_a = A_b = A$.

$$\begin{cases} V_a = V_{a0} + A * (0.1 + y), \\ V_b = V_{b0} + A * (0.1 - y). \end{cases} \tag{36}$$

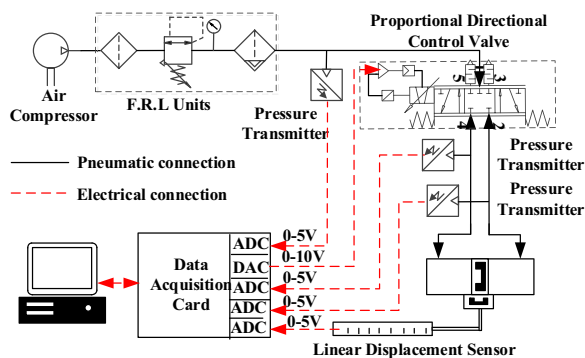


Figure 13 Working principle of servo system of magnetically coupled nonlinear rodless cylinder position

According to Newton’s second law, the dynamic equation for a magnetically coupled rodless cylinder is expressed as follows:

$$A(P_a - P_b) = ma + F_f, \tag{37}$$

where A is the effective area of the piston, and its value is 490.87 mm^2 ; m is the load quality; a is the acceleration of the cylinder running; V_{a0} is the remnant volume in cavity A, and its value is 7363 mm^3 ; V_{b0} is the remnant volume in cavity B, and its value is 7363 mm^3 .

4 Establishment of Experimental Platform

The working principle of the servo system of the magnetically coupled nonlinear rodless cylinder position is illustrated in Figure 13.

The components of the magnetically coupled nonlinear rodless cylinder position servo system are listed in Table 3.

The gas was first produced by an air compressor and passed through a pneumatic triplet (air filter [F], pressure-reducing valve [R], and oil mist [L]), which purified and filtered the entering gas and reduced the rated pressure. Three pressure transmitters connected before

and after the proportional directional control valve were used to determine the gas pressures of the gas source and the two cavities of the magnetically coupled rodless cylinder. The flow direction and size of the gas after passing through the proportional directional control valve changed with the displacement of the proportional directional control valve spool. When applying a 0–5 V digital voltage signal to the proportional directional control valve, the acquisition card converted the digital voltage signal into a 0–5 V analog voltage signal to the proportional directional control valve, and the spool moved to the left. When a 5–10 V digital voltage signal was applied to the proportional direction control valve, the acquisition card transferred the digital voltage signal into a 5–10 V analog voltage signal to the proportional directional control valve, and the spore moved to the right. The changes in the flow direction and size of the gas at the proportional directional control valve outlet changed the movement direction and speed of the piston in the cylinder. A linear displacement sensor was connected to the slider of the magnetically coupled rodless cylinder through an iron plate. The linear displacement sensor could be driven when the slider of the magnetically coupled rodless cylinder moved.

Therefore, the linear displacement sensor could measure the moving distance of the slider in the cylinder in real time. The data acquisition card converted the displacement analog voltage signal into a digital signal, which could be displayed on a computer. Figure 14 shows the construction diagram of the experimental platform.

The corresponding simulation model diagrams are shown in Figure 15. The model consisted of two parts. The valve portion received voltage and pressure signals and generated mass flow signals to the cylinder. The cylinder portion received the mass flow signals and generated pressure, acceleration, speed, and distance signals.

Table 3 Components of experimental platform

Component	Model	Parameter
Air compressor	HX750A	Maximum supply pressure 1.0 MPa
F.R.L units	AF/L/U2000	Maximum working pressure 1.0 MPa
Proportional Directional control Valve	FESTO MPYE-5-M5-010-B	Maximum working pressure 1.0 MPa
Magnetically Coupled rodless Cylinder	CY3R25-200	Maximum working pressure 0.7 MPa
Linear displacement Sensor	KTC-200	Measuring range 200 mm, linear precision 0.05%
Pressure transmitter	MIK-P300	Measuring range –0.1~60 MPa
Data acquisition Card	NI PCIE-6353	16-bit counter, –10V to 10V output voltage
Personal computer	B560-A Chip Board	Standard configuration

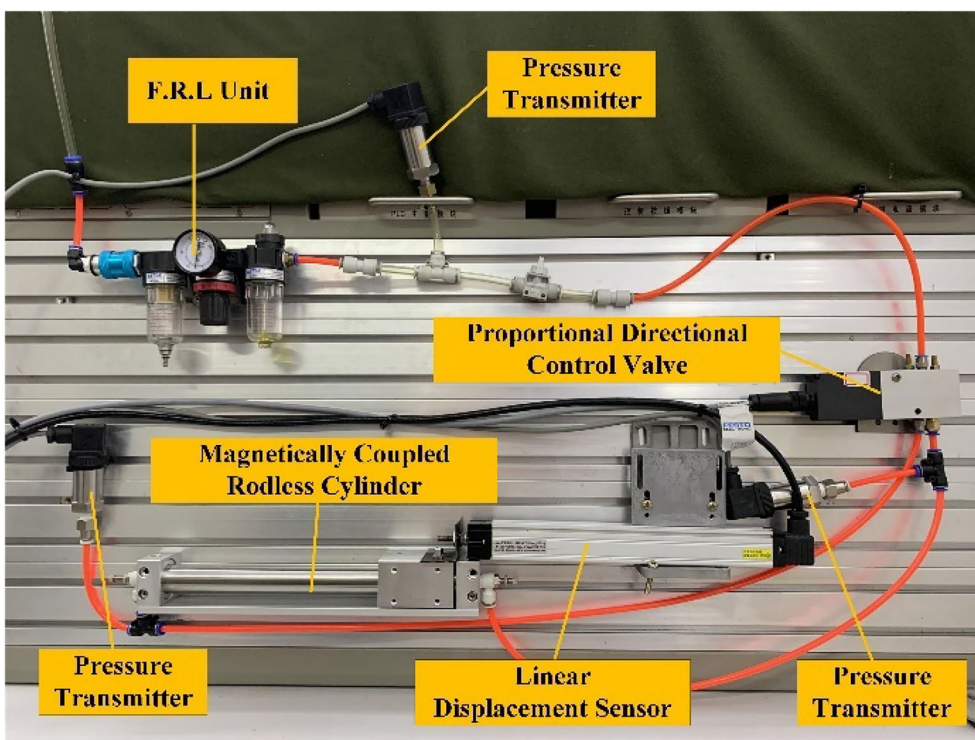


Figure 14 Experimental platform

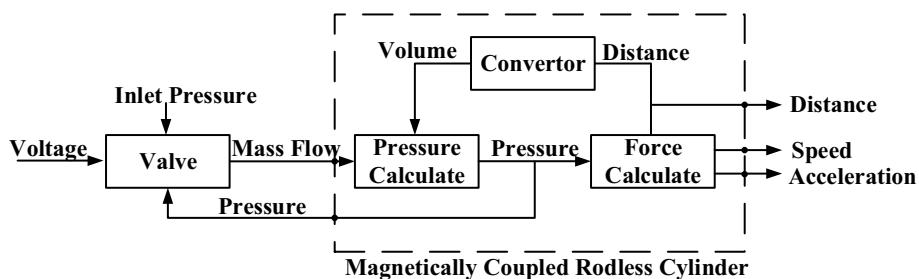


Figure 15 Corresponding simulation model of valve-control cylinder system

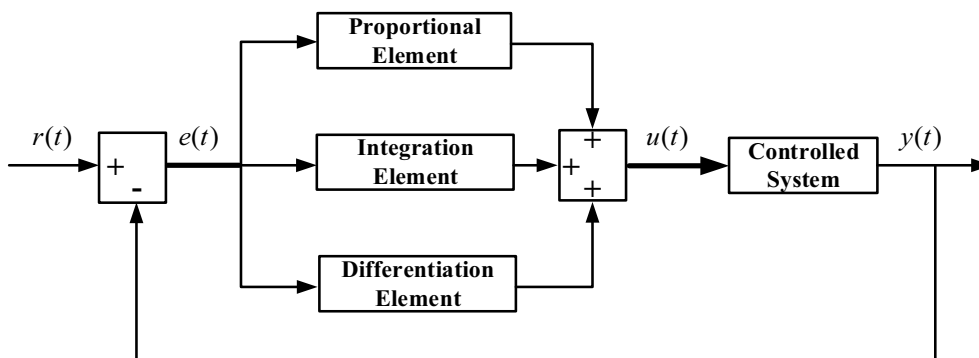


Figure 16 Structure of PID control system

5 Pneumatic Servo Control System

5.1 Incremental PID Control Algorithm

PID control has always been the most widely used control algorithm [18] because it has simple control principles, strong adaptability, and robustness. Figure 16 shows the structure of the PID control system.

The control law of the incremental PID control system is expressed as follows:

$$\Delta u(k) = K_p(e(k) - e(k - 1)) + K_i e(k) + K_d(e(k) - 2e(k - 1) + e(k - 2)), \quad (38)$$

where K_p is the proportional coefficient; K_i is the integral coefficient; K_d is the differential coefficient, and $e(k)$ is the input and output error at the k moment.

A pneumatic circuit (Figure 14) was developed to verify the accuracy of the nonlinear mathematical model of the magnetically coupled rodless cylinder. The mathematical model of the magnetically coupled nonlinear rodless cylinder position servo system should be verified experimentally.

Because the application of the magnetically coupled rodless cylinder is mostly moved at a number of fixed points, given a cycle of 20 s, pulse width of 50%, height of 0.18, delay of 2 s pulse signal, and downward bias of 0.09, its physical significance is to make the cylinder with the stroke the origin every 10 s at an upward or downward swing of 0.09 m. The air-source pressure was constant (0.5 MPa).

An incremental PID control was used as the control strategy for the system. Table 4 lists the optimized parameters.

The environmental correction parameter, C , was obtained to make the simulation model more realistic, and the dichotomy method was used for experimental correction.

The real-time error between the simulation model and the experimental platform when stable is shown in Figure 17. When $C=0.6250$ was used, the average error was 0.005175054 (m), which was approximately 2.588% of the total travel distance when the parameters were corrected.

The optimal simulation curve and experimental results are shown in Figure 18. Input_Sig is the input signal, Exp_Sig is the real-time position of the experimental platform, Sim_Sig is the position output of the simulation

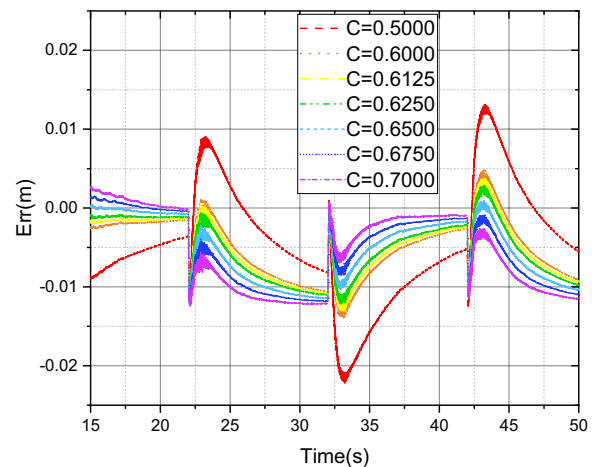


Figure 17 Real-time error between simulation model and experimental platform

model, Exp_Voltage is the real-time voltage of the experimental platform, and Sim_Voltage is the output voltage of the simulation model.

The reasons for the error between the optimal simulation curve and the experimental results are as follows.

- (1) The simulation model was run from the middle of the cylinder, whereas the experimental model was run from the end.
- (2) During the experimental process, the friction coefficient was varied, and the positive and negative strokes were asymmetric, whereas a fixed friction coefficient was used in the modeling and simulation. Therefore, a displacement error was observed.
- (3) Gas leakage occurred in the gas path and cylinder.
- (4) The air supply pressure was unstable.

5.2 Setting PID Control Algorithm Based on RBF Neural Network

Artificial neural networks are control algorithms that process information by mimicking animal neural networks. In 1943, psychologist Macculloch and mathematician Pitts first proposed a mathematical model of neurons [19]. Later, Powell [20] proposed the radial basis function in 1988, and Broomhead and Lowe applied the RBF to neural network design for the first time [21]. Compared with backpropagating (BP) neural networks, RBF neural networks have the advantage of high learning efficiency and are gradually replacing BP neural networks in certain fields. The hidden layer space in the RBF neural network is composed of the “basis” of the hidden layer units. The hidden layer transforms the low-dimensional vector input from the input layer to a high-dimensional space such that the linear nonseparable problems in the

Table 4 Optimized parameters

Symbol	Physical significance	Value
K_p	Proportional coefficient	8
K_i	Integration coefficient	0.00001
K_d	Differentiation coefficient	0.0001

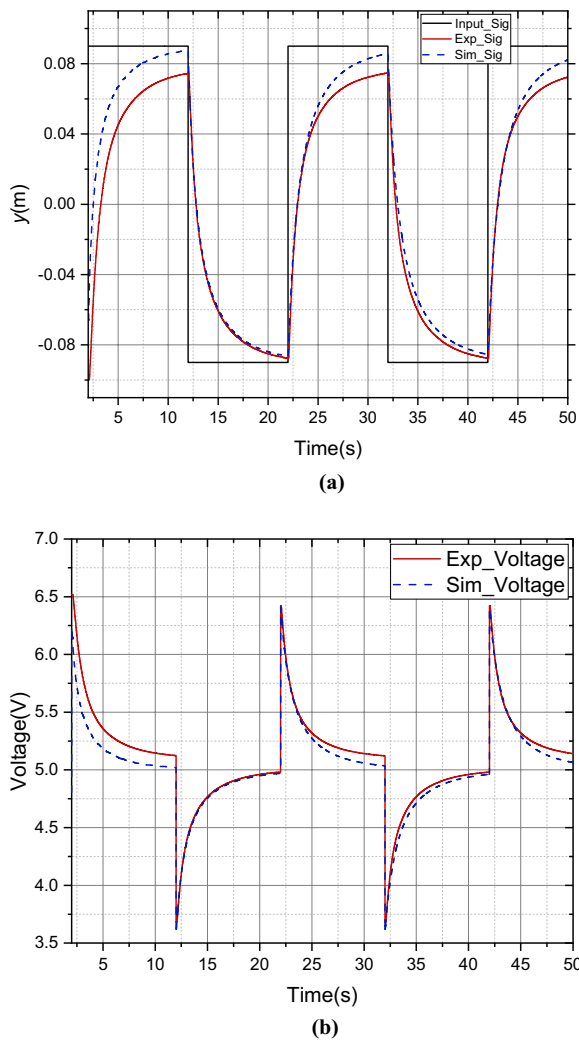


Figure 18 (a) Comparison between experimental real-time position and simulation output results, (b) Comparison between experimental voltage and simulation voltage results

low-dimensional space can be linearly separable in a high-dimensional space [22].

RBF neural network controller has three layers: input, hidden, and output. The input layer consists of nodes of the signal source, and its main function is to connect the outside world to the neural network. The number of nodes in the hidden layer is determined by a specific problem, and a nonlinear transformation can be performed from the input layer to the hidden layer. The number of nodes in the output layer is also determined by the specific output requirements, which primarily apply a response to the activation signal of the output layer, as shown in Figure 19.

5.2.1 Composition of RBF Neural Network

RBF neural network mainly consists of the following two mappings.

The first is a nonlinear mapping from the input layer to the hidden layer, which mainly maps the N -dimensional data of the input layer to the m -dimensional space of the hidden layer to achieve mapping from X to h_j . The mathematical expression for the radial basis vector is as follows:

$$h_j = f_j(x_1, x_2, \dots, x_n), \tag{39}$$

where f_j is the RBF, and $j = 1, 2, 3, \dots, m$.

The selected radial basis function is a Gaussian function, expressed by Eq. (40):

$$f(X) = \exp\left(-\frac{\|X - c_j\|^2}{b_j^2}\right), b_j > 0, x \in R, \tag{40}$$

where c_j is the central point of the neuron in the hidden layer j , $c_j = [c_{j1}, \dots, c_{jn}]$, and b is the width vector of the Gaussian function, $b = [b_1, \dots, b_m]^T$.

The second mapping is linear from the hidden layer to the output layer, which sums and calculates the space vector of the m -dimension of the hidden layer with linear weighting and transmits it to the output layer for output. The expression for mapping h_j to y_m is as follows:

$$y_m = \sum_j^m w_j h_j. \tag{41}$$

5.2.2 Parameter Modification of RBF Neural Network

In the control strategy of an RBF neural network, the center c_j , width b , and weight W of the basis function must be adjusted. Before adjusting the parameters, the performance index function is defined as follows:

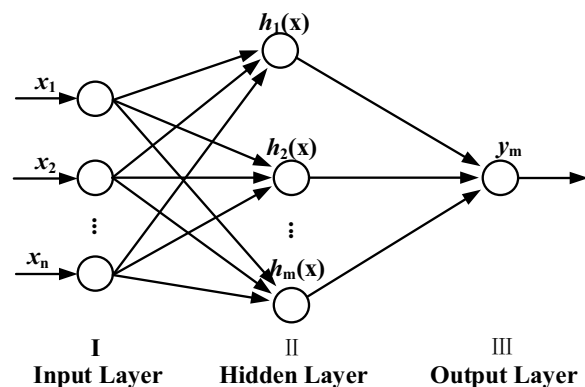


Figure 19 Model of RBF neural network

$$J = \frac{1}{2}(y(k) - y_m(k))^2, \tag{42}$$

where $y(k)$ is the input to the network at time k , and $y_m(k)$ is the network output at time k .

Based on the gradient descent method, the modified formula for the weight W is as follows:

$$\Delta\omega_j(k) = -\frac{\partial J}{\partial\omega_j(k-1)} = (y(k) - y_m(k))h_j, \tag{43}$$

$$w_j(k) = w_j(k-1) + \eta\Delta\omega_j(k) + \alpha(w_j(k-1) - w_j(k-2)). \tag{44}$$

The modified formula for $c_{ji}(k)$ is as follows:

$$\Delta c_{ji} = -\frac{\partial J}{\partial c_j} = (y(k) - y_m(k))w_j \frac{x - c_{ji}}{b_j^2}, \tag{45}$$

$$c_{ji}(k) = c_{ji}(k-1) + \eta\Delta c_{ji} + \alpha(c_{ji}(k-1) - c_{ji}(k-2)). \tag{46}$$

The modified formula for $b_j(k)$ is as follows:

$$\Delta b_j = -\frac{\partial J}{\partial b_j} = (y(k) - y_m(k))w_j h_j \frac{\|x - c_j\|^2}{b_j^3}, \tag{47}$$

$$b_j(k) = b_j(k-1) + \eta\Delta b_j + \alpha(b_j(k-1) - b_j(k-2)). \tag{48}$$

5.2.3 Adjusting PID Controller Parameters

The control error of the incremental PID controller is expressed as follows:

$$e(k) = r(k) - y(k). \tag{49}$$

The input of the controller is defined as follows:

$$x_{c1}(k) = e(k) - e(k-1), \tag{50}$$

$$x_{c2}(k) = e(k), \tag{51}$$

$$x_{c3}(k) = e(k) - 2e(k-1) + e(k-2). \tag{52}$$

The output increment is defined by Eq. (53):

$$u(k) = u(k-1) + \Delta u(k). \tag{53}$$

The training index of the RBF neural network is expressed as follows:

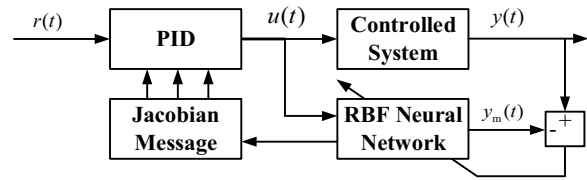


Figure 20 RBF PID control process

Table 5 Parameters of RBF PID control

Physical significance	Symbol	Value
Learning rate	lr	0.1
Factor of momentum	β	0.06
Number of neurons	nn	6
Initial PID parameter	K_p	8
	K_i	0.00001
	K_d	0.0001
PID parameter learning rate	lr_K_p	0.08
	lr_K_i	0.00001
	lr_K_d	0.0001

$$E(k) = \frac{1}{2}e(k)^2. \tag{54}$$

The gradient descent method [23, 24] was used to adjust the PID control parameters, as follows:

$$\begin{aligned} \Delta K_p &= -\eta_p \frac{\partial E}{\partial K_p} = -\eta_p \frac{\partial E}{\partial y} \frac{\partial y}{\partial u} \frac{\partial \Delta u}{\partial K_p} \\ &= \eta_p e(k) \frac{\partial y}{\partial u} x_{c1}(k), \end{aligned} \tag{55}$$

$$\begin{aligned} \Delta K_i &= -\eta_i \frac{\partial E}{\partial K_i} = -\eta_i \frac{\partial E}{\partial y} \frac{\partial y}{\partial u} \frac{\partial u}{\partial K_i} \\ &= \eta_i e(k) \frac{\partial y}{\partial u} x_{c2}(k), \end{aligned} \tag{56}$$

$$\begin{aligned} \Delta K_d &= -\eta_d \frac{\partial E}{\partial K_d} = -\eta_d \frac{\partial E}{\partial y} \frac{\partial y}{\partial u} \frac{\partial u}{\partial K_d} \\ &= \eta_d e(k) \frac{\partial y}{\partial u} x_{c3}(k), \end{aligned} \tag{57}$$

where η_p, η_i, η_d are the learning efficiencies of K_p, K_i, K_d , respectively, and represent the Jacobian information of magnetically coupled rodless cylinder. Its expression is as follows:

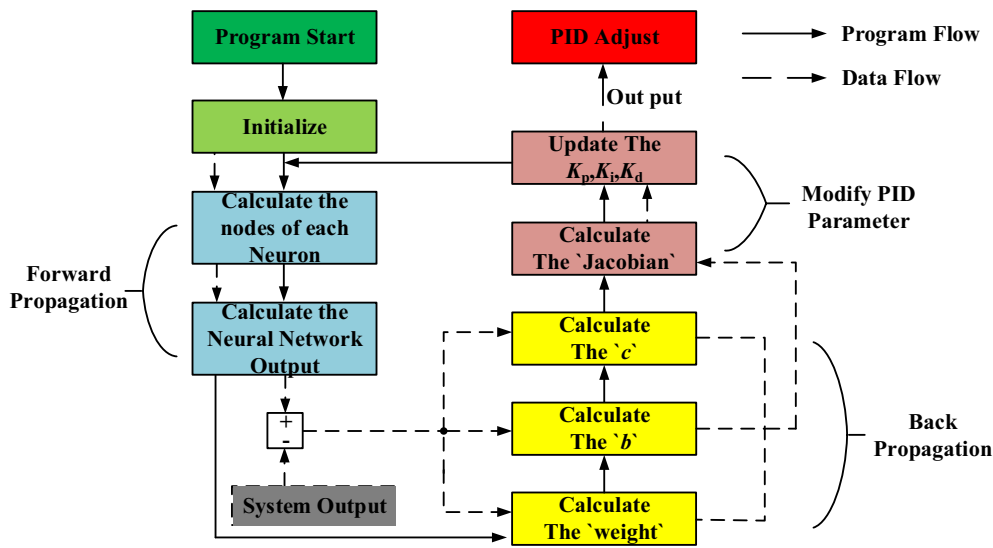


Figure 21 Flowchart of change in RBF neural network parameters

$$\frac{\partial y(k)}{\partial u(k)} \approx \frac{\partial y_m(k)}{\partial u(k)} = \sum_{j=1}^m w_j h_j \frac{c_j - x_1}{b_j^2}. \tag{58}$$

5.2.4 Positioning Experiment Based on RBF Neural Network Setting PID Controller

The overall control process is shown in Figure 20, and Table 5 lists the parameters.

The parameters were then modified, as shown in Figure 21. First, the program was initialized. Second, the nodes of each neuron and the neural network output were calculated. Third, the system output was used to recalculate the data of “c”, “b”, and “weight.” Finally, the “Jacobian” and K_p, K_i, K_d were calculated.

The PID control model was compared with the RBF-tuning PID control model, and the input-output curves were plotted, as shown in Figure 22. The PID parameter correction curve is shown in Figure 23. The PID parameters changed with time.

The response error of the system is shown in Figure 24. After a period of online learning, the control system using the RBF-setting PID method became better than the incremental PID control system in terms of approaching speed.

A sinusoidal signal was used to assess the performance. The amplitude of the input signal was 0.09, and the period was 2 s/rad. The values of the parameters are listed in Table 6.

A comparison of the two control methods is shown in Figure 25.

Figure 26 presents the PID parameter correction curve for the sinusoidal signal. When a sinusoidal signal is used as the input signal, the RBF-tuning PID method becomes better than the incremental PID method in terms of approaching speed.

6 Conclusions and Further Work

In this paper, the proportional directional control valve and the magnetically coupled rodless cylinder were used as the research object to achieve the precise positioning of magnetically coupled rodless cylinder. In addition, the pneumatic position servo experimental platform was established. The following conclusions were drawn.

- (1) The factors influencing the magnetically coupled nonlinear rodless cylinder position servo system were analyzed, and an experimental test platform was built to examine the characteristics and physical structure of the main components of the experimental system.
- (2) A theoretical model of the magnetically coupled nonlinear rodless cylinder position servo system was developed in MATLAB based on the theoretical and experimental data.
- (3) An experimental platform for the magnetically coupled nonlinear rodless cylinder position servo system was constructed.
- (4) Simulation and physical models were compared using incremental PID control, and the accuracy

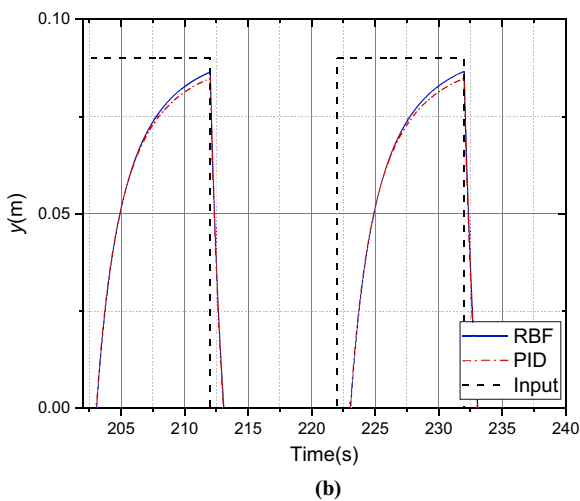
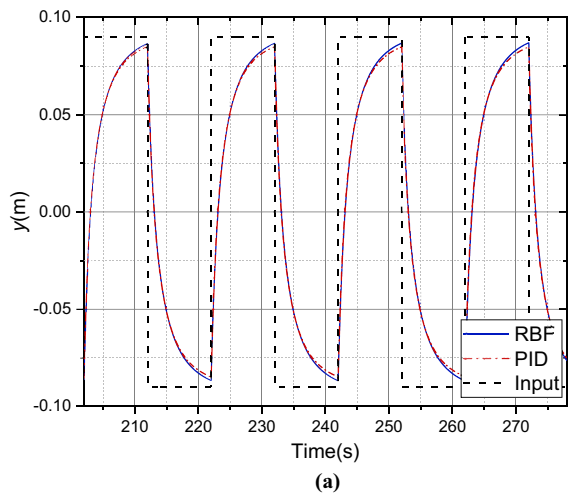


Figure 22 Input–output comparison between RBF-PID and PID control methods: (a) Curves, (b) Zoomed graph

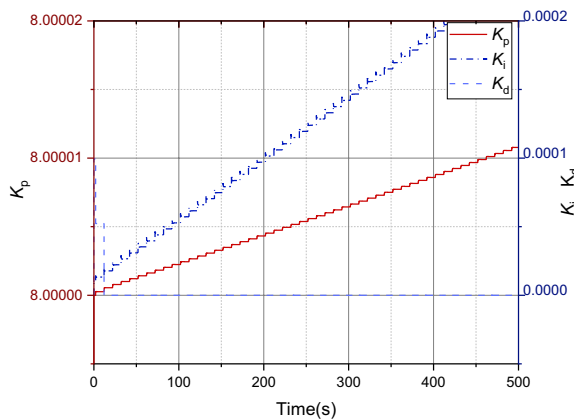


Figure 23 Parameter change curve of RBF setting PID

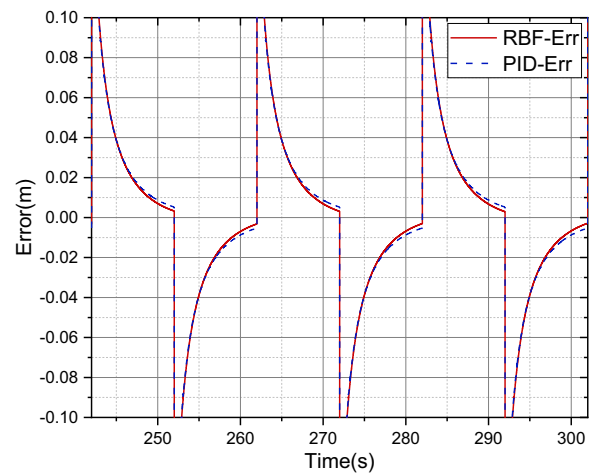


Figure 24 Response error of system

Table 6 Parameters set for sinusoidal signal

Physical significance	Symbol	Value
Learning rate	lr	0.2
Factor of momentum	β	0.06
Number of neurons	nn	6
Initial PID parameter	K_p	30
	K_i	0.00001
	K_d	0.0001
PID parameter learning rate	lr_{K_p}	0.4
	lr_{K_i}	0.02
	lr_{K_d}	0.02

and validity of the mathematical models were verified. The mean error of 0.005175054 (m) is approximately 2.588% of the total stroke.

- (5) An approach to control the motion of the magnetically coupled rodless cylinder based on an RBF neural network to set the PID parameters was proposed to compare the experimental results with those of the incremental PID.
- (6) The results show that the RBF neural network-tuning PID method is better than the simple incremental PID control method in controlling the precision and response speed.

However, the heat exchange process between the gas in the cylinder and the external environment was neglected. There is room for improvement in this regard. Further work should include other control algorithms combined with an RBF neural network-tuning PID-control algorithm

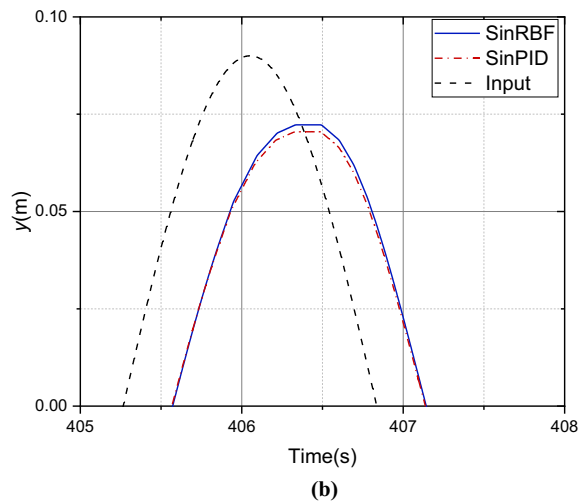
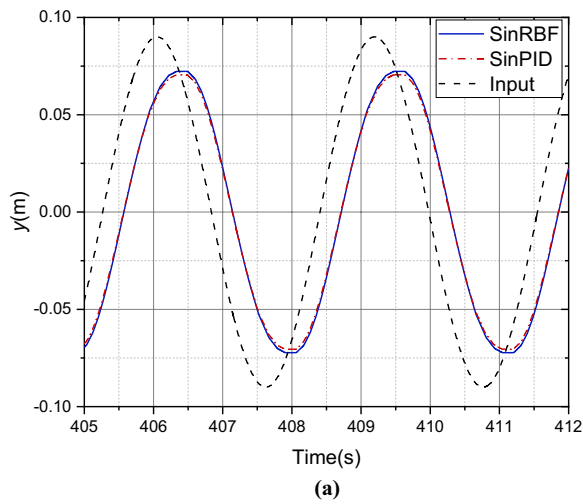


Figure 25 Comparison of two control methods: (a) The plots, (b) Zoomed graph

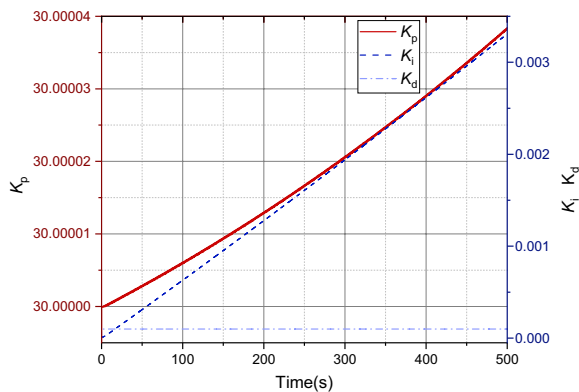


Figure 26 PID parameter correction curve for sinusoidal signal

or the design of a new composite control method that will improve the accuracy of magnetically coupled nonlinear rodless cylinder position servo systems.

Acknowledgments

Not applicable.

Authors' Contributions

YZ was in charge of the whole trial; DK wrote the manuscript; DK and GJ assisted with sampling and laboratory analyses. YZ, YS, SL, BL and MC revised the manuscript, performed the experiments and analyzed the data. All authors read and approved the final manuscript.

Authors' Information

Yeming Zhang, born in 1979, is currently an associate professor at Henan Polytechnic University, China. He received his PhD degree from Beihang University, China, in 2011. His research interests include complex mechatronics system simulation system simulation, design, intelligent control, reliability and fault diagnosis, pneumatic system saving and flow measurement.

Demin Kong, born in 1997, is currently a master candidate at Henan Polytechnic University, China.

Gonghua Jin, born in 1997, is currently a master candidate at Henan Polytechnic University, China.

Yan Shi, born in 1981, is a full professor at School of Automation Science and Electrical Engineering, Beihang University, China. He received his doctoral degree in mechanical engineering from Beihang University, China. His research interests include mechatronic engineering, intelligent medical devices and energy-saving technologies of pneumatic systems.

Maolin Cai, born in 1972, is currently a professor and a PhD candidate supervisor at Beihang University, China. He received his PhD degree from Tokyo Institute of Technology, Japan, in 2002. His research interests include pneumatic system saving, simulation, control and flow measurement.

Shuping Li, born in 1976, is currently a lecturer at Henan Polytechnic University, China. He received his PhD degree from Shanghai University, China, in 2013. His research interests include machine vision and bionic eye technology.

Baozhan Lv, born in 1973, is currently a professor at Henan Polytechnic University, China. He received his PhD degree from Nanjing Agricultural University, China, in 2008. His research interests include vehicle system dynamics and control, new energy vehicle technology and mining machinery design and manufacturing.

Funding

Supported by Outstanding Young Scientists in Beijing of China (Grant No. BJJWZYJH01201910006021), Open Foundation of the State Key Laboratory of Fluid Power and Mechatronic Systems of China (Grant No. GZKF-202016), Henan Provincial Science and Technology Key Project of China (Grant Nos. 202102210081, 212102210050), Sub Project of Strengthening Key Basic Research Projects in the Basic Plan of the Science and Technology Commission of the Central Military Commission of China (Grant No. 2019-JCJQ-ZD-120-13), Henan Provincial Fundamental Research Funds for the Universities of China (Grant No. NSFRF200403).

Availability of data and materials

The datasets used and/or analyzed during the current study are available from the corresponding author on reasonable request.

Declarations

Ethics approval and consent to participate

Not applicable.

Competing interests

The authors declare no competing financial interests.

Received: 13 May 2022 Revised: 25 October 2023 Accepted: 31 October 2023

Published online: 04 December 2023

References

- [1] Z H Rao, G M Bone. Nonlinear modeling and control of servo pneumatic actuators. *IEEE Transactions on Control Systems Technology*, 2008, 16(3): 562-569.
- [2] L W Lee, I H Li. Wavelet-based adaptive sliding-mode control with H_{∞} tracking performance for pneumatic servo system position tracking control. *IET Control Theory & Applications*, 2012, 6(11): 1699-1714.
- [3] Y M Zhang, K M Li, M Xu, et al. Medical grabbing servo system with friction compensation based on the differential evolution algorithm. *Chinese Journal of Mechanical Engineering*, 2021, 34: 107.
- [4] Y H Bai. *Pneumatic servo system analysis and control*. Beijing: Metallurgical Industry Press, 2014.
- [5] H P Ren, J T Fan. Adaptive backstepping slide mode control of pneumatic position servo system. *Chinese Journal of Mechanical Engineering*, 2016, 29(5): 1003-1006.
- [6] I H Li, H H Chiang, L W Lee. Development of a linear delta robot with three horizontal-axial pneumatic actuators for 3-DOF trajectory tracking. *Applied Sciences*, 2020, 10(10): 3526.
- [7] S C Hsu, C Y Lin. Periodic motion control of a heavy duty pneumatic actuating table using low cost position sensors and hybrid repetitive control. *IEEE International Symposium on Industrial Electronics*, Taipei, China, 2013: 641-646.
- [8] S J Huang, H W Shieh. Motion control of a nonlinear pneumatic actuating table by using self-adaptation fuzzy controller. *Advanced Science Letters*, 2009: 1-6.
- [9] SMC China Co, Ltd. *Modern practical pneumatic technology*. 2nd ed. Beijing: China Machine Press, 2004.
- [10] Y B Wang. *Research on tracking control three axis pneumatic servo system*. Harbin: Harbin Institute of Technology, 2008 (in Chinese).
- [11] M L Cai. Modern pneumatic technology theory and practice lecture 1: Flow characteristics of pneumatic components. *Hydraulics Pneumatics & Seals*, 2007, 2: 44-48.
- [12] Z S WU. *Pneumatic transmission and control*. Harbin: Harbin Institute of Technology Press, 2009.
- [13] Y Y Zhang. *Fluid Mechanics*. 2nd edition. Beijing: Higher Education Press, 1999.
- [14] J Sifuentes-Mijares, V Santibáez, J L Meza-Medina. Nonlinear PID global regulators with self-tuned PD gains for robot manipulators: theory and experimentation. *Journal of the Brazilian Society of Mechanical Sciences and Engineering*, 2021, 43(4): 223.
- [15] P Qian, C Pu, L Liu, et al. Development of a new high-precision friction test platform and experimental study of friction characteristics for pneumatic cylinders. *Measurement Science and Technology*, 2022, 33(6): 065001.
- [16] J F Li. *Dynamics of pneumatic transmission system*. Changsha: South China University of Technology Press, 1991.
- [17] M L Cai. Modern pneumatic technology theory and practice lecture 5: Characteristics of cylinder drive systems. *Hydraulics Pneumatics & Seals*, 2007, 27(6): 55-58.
- [18] K A Al Sumarmad, N Sulaiman, N I A Wahab, et al. Energy management and voltage control in microgrids using artificial neural networks, PID, and fuzzy logic controllers. *Energies*, 2022, 15(1): 303.
- [19] W S McCulloch, W Pitts. A logical calculus of the ideas imminent in nervous activity. *Bulletin of Mathematical Biophysics*, 1973, 5(4): 115-133.
- [20] M J D Powell. Radial basis function for multivariable interpolation. *IMA Conference on Algorithms for the Approximation of Functions and Data*. RMCS, 1985.
- [21] D S Broomhead, D Lowe. Multivariable functional interpolation and adaptive networks. *Complex Systems*, 1988, 2: 321-355.
- [22] H W Zhao, R Li. Typical adaptive neural control for hypersonic vehicle based on higher-order filters. *Journal of Systems Engineering and Electronics*, 2020, 31(5): 1031-1040.
- [23] C Chen, J Q Xu, W Ji, et al. Sliding mode robust adaptive control of maglev vehicle's nonlinear suspension system based on flexible track: Design and experiment. *IEEE Access*, 2019, 7(7): 41874-41884.
- [24] T Q Xiao, Z Wu, P D Christofides, et al. Recurrent neural-network-based model predictive control of a plasma etch process. *Industrial & Engineering Chemistry Research*, 2021, 61(1): 638-652.

Submit your manuscript to a SpringerOpen[®] journal and benefit from:

- Convenient online submission
- Rigorous peer review
- Open access: articles freely available online
- High visibility within the field
- Retaining the copyright to your article

Submit your next manuscript at ► [springeropen.com](https://www.springeropen.com)
